*International Journal of Minerals, Metallurgy and Materials*
*Volume 27, Number 2, February 2020, Page 190*
**https://doi.org/10.1007/s12613-019-1876-8**

# Thermal and microstructural characterization of a novel ductile cast iron modified by aluminum addition

*Gülşah Aktaş Çelik*[1)], *Maria-Ioanna T. Tzini*[2)], *Şeyda Polat*[1)], *Ş. Hakan Atapek*[1)], *and Gregory N. Haidemenopoulos*[2,3)]

1) Department of Metallurgical and Materials Engineering, Kocaeli University, Kocaeli 41001, Turkey
2) Laboratory of Materials, Department of Mechanical Engineering, University of Thessaly, Volos 383 34, Greece
3) Department of Mechanical Engineering, Khalifa University of Science and Technology, Abu Dhabi 127788, UAE
(Received: 4 March 2019; revised: 19 April 2019; accepted: 9 May 2019)

**Abstract:** In high-temperature applications, like exhaust manifolds, cast irons with a ferritic matrix are mostly used. However, the increasing demand for higher-temperature applications has led manufacturers to use additional expensive materials such as stainless steels and Ni-resist austenitic ductile cast irons. Thus, in order to meet the demand while using low-cost materials, new alloys with improved high-temperature strength and oxidation resistance must be developed. In this study, thermodynamic calculations with Thermo-Calc software were applied to study a novel ductile cast iron with a composition of 3.5wt% C, 4wt% Si, 1wt% Nb, 0–4wt% Al. The designed compositions were cast, and thermal analysis and microstructural characterization were performed to validate the calculations. The lowest critical temperature of austenite to pearlite eutectoid transformation, i.e., $A_1$, was calculated, and the solidification sequence was determined. Both calculations and experimental data revealed the importance of aluminum addition, as the $A_1$ increased by increasing the aluminum content in the alloys, indicating the possibility of utilizing the alloys at higher temperature. The experimental data validated the transformation temperature during solidification and at the solid state and confirmed the equilibrium phases at room temperature as ferrite, graphite, and MC-type carbides.

**Keywords:** ductile cast iron; alloy design; Thermo-Calc; high-temperature material

## 1. Introduction

Exhaust manifolds deliver hot exhaust gases from the combustion chamber to the atmosphere [1]. In new engine designs that satisfy environmental and fuel consumption regulations [2], exhaust gas temperature can reach 1000°C. The exhaust manifolds are exposed to elevated temperature for a long time and to continuous thermal cycles during the engine operation. Moreover, severe high-temperature oxidation occurs due to hot exhaust gas flow. Therefore, mechanical stability, thermal fatigue resistance, and low thermal expansion of the material are significant criteria. High thermal conductivity and low thermal expansion coefficient reduce the stress produced in the component during the start-up and shutdown of the engine [1–5].

Due to the increase in exhaust gas temperature, manufacturers are in search of new materials that can withstand thermal and mechanical stresses and an oxidative environment [2–10]. In contrast to ferritic ductile cast irons, the development of new austenitic stainless steels and Ni-resist austenitic ductile cast irons are in demand due to the high thermal stability of the austenitic matrix [2,5,11]. However, these austenitic alloys are more expensive because of their chemical composition and manufacturing process. To meet the demand while using low-cost materials, new alloys with improved high-temperature strength and oxidation resistance must be developed [12–13]. Ekström and Jonsson showed that ferritic alloys have higher thermal conductivity and lower thermal expansion than austenitic alloys [3]. Nevertheless, the $A_1$ temperature of SiMo alloy, which determines the limit of its service temperature, is approximately 820°C [4], and the elastic modulus of SiMo51 decreases above 700°C

Corresponding author: Gülşah Aktaş Çelik E-mail: gulsahaktas@gmail.com

[3]. Therefore, it is reasonable to develop a ferritic ductile cast iron with a higher $A_1$ temperature in order to enhance both thermal and mechanical properties at higher temperature. In the alloy design of ductile cast iron, high graphite nodularity, high nodule count, and homogeneous graphite distribution can be obtained with hypereutectic composition; thus, C and Si should be selected to obtain a hypereutectic C equivalent (≥4.7) for casting and solidification [14]. To increase the $A_1$ temperature, besides Si, other alloying elements such as Al, Ti, Nb, and W may be added to the composition [15–16]. Aluminum also increases the oxidation resistance by forming a stabilized oxide layer at elevated temperature [6,17]. Mechanical properties can be enhanced by the addition of carbide-forming elements such as Mo [6], Ti [18], Nb [19], W [20], and Cr [21] up to 1wt% [6]. Among these, Ti and Nb enhance mechanical properties at elevated temperature by forming primary carbides that are stable at these temperatures [22–23]. However, their presence is well known to change the graphite morphology from spheroidal to vermicular [24–27], and as a result, the mechanical properties are lowered [28–29], but thermal conductivity is improved [30].

It is important to obtain information about the effects of alloying elements on transformation temperature and thermal and mechanical properties before the alloys are actually produced [31–34]. CALPHAD-based approaches have been used to provide such information and predict the transformation temperature, thermal expansion, type and amount of phases stable at studied temperature, solidification sequence, and the oxide phases formed at any given temperature for the designed alloy composition [35–36]. Thus, it is important to perform such thermodynamic calculations as preliminary studies in order to determine the type and amount of the alloying elements.

In this study, thermodynamic calculations employing Thermo-Calc software were applied to study a novel ductile cast iron with a composition of 3.5wt% C, 4wt% Si, 1wt% Nb, and 0–4wt% Al to reveal the possibility of its use in the place of commercial ferritic ductile cast irons at more demanding working condition. The designed compositions were cast, and thermal analysis and microstructural characterization were performed to verify the thermodynamic calculations.

## 2. Methodology

### 2.1. Computational method

Thermodynamic calculations to study cast iron with a composition of 3.5wt% C, 4wt% Si, 1wt% Nb, and 0–4wt% Al were carried out with Thermo-Calc software. To determine the $A_1$ temperature of the studied compositions, the TCFE6 database was used. The solidification sequence of the compositions, which is important for castability, was studied using the Scheil module.

### 2.2. Experimental procedure

After calculations, the alloys were produced as Y blocks by sand casting according to American Society for Testing Materials (ASTM) A536-84 standard. For this process, a 5 kg charge was prepared with nodular pig iron (4.30wt% C and 0.7wt% Si), ferrosilicon (72wt% Si), ferroniobium (70wt% Nb), and DIN 1020 steel. The charge was melted in a 35 kW Inductotherm Induction Furnace with a capacity of 25 kg. Just before the melting process was complete, pure aluminum was added according to the chosen composition. The melting process was completed at 1560°C and was followed by a spheroidization process, which was carried out in a SiC crucible. For the spheroidization process, a nucleation agent (75wt% Si, 0.94wt% Ca, 1.68wt% Ce, and 0.89wt% Al) and a magnesium-rich alloy FeSiMg (45wt% Si and 7wt% Mg) for spheroidization were placed at the bottom of the crucible before the charge was poured. After the spheroidization, a sample from the molten alloy was taken by pouring it into a copper mold, and its chemical composition was verified using optical emission spectrometry (OES, Foundry Master). The rest of the molten metal was cast into a sand mold prepared as a Y block according to ASTM A536-84 standard. Table 1 presents the chemical compositions of the cast alloys, which are in the required range as designed. The main composition (3.5wt% C, 4wt% Si, and 1wt% Nb) is coded as specimen 0Al, and the others are coded as 1Al, 2Al, 3Al, and 4Al for 1wt%, 2wt%, 3wt%, and

**Table 1. Chemical compositions of the cast alloys obtained by OES** wt%

| Alloy | C | Si | Nb | Al | Mg | Mn | P | S |
|---|---|---|---|---|---|---|---|---|
| 0Al | 3.57 | 4.04 | 0.96 | 0.02 | 0.074 | 0.231 | 0.0579 | 0.0282 |
| 1Al | 3.46 | 3.96 | 0.97 | 0.97 | 0.082 | 0.235 | 0.0597 | 0.0285 |
| 2Al | 3.47 | 3.99 | 1.03 | 2.03 | 0.078 | 0.245 | 0.0572 | 0.0321 |
| 3Al | 3.52 | 4.07 | 1.02 | 3.05 | 0.081 | 0.225 | 0.0581 | 0.0287 |
| 4Al | 3.54 | 4.05 | 1.04 | 4.03 | 0.079 | 0.228 | 0.0558 | 0.0355 |

4wt% Al additions, respectively.

Both microstructural examinations and thermal analysis were applied to the cast alloys to validate the computational results in terms of (1) the phases formed during solidification, (2) critical temperature, and (3) the phases stable at the room temperature (RT). For microscopic examinations, as-cast alloys were prepared by metallographic methods and etched by both Nital (3vol% $HNO_3$) and a color etchant containing 10 g picric acid, 10 g NaOH, 40 g KOH, and 50 mL distilled water. The color etching process was carried out at 100°C for 20 min. Microstructural characterization was carried out using light microscopy (LM, Olympus BX41M-LED), scanning electron microscopy (SEM, JEOL JSM 6060), and energy dispersive spectrometry (EDS, IXRF). The phases were also identified using X-ray diffraction (XRD, Rigaku Ultima+), carried out with Cu $K_\alpha$ radiation and a scanning speed of 1.0°·min$^{-1}$. The determined phases were quantified according to International Standards Organisation (ISO) 945-2, using an image analyzer (Leica Las V4.12). Thermal analysis was carried out using differential thermal analysis (DTA, Netzsch STA 409 PG Luxx). The DTA samples were heated to 1460°C at a rate of 5°C·min$^{-1}$, held at that temperature for 5 min, and then cooled to RT at a rate of 5°C·min$^{-1}$. For mechanical characterization, hardness measurement was carried out using micro Vickers (EmcoTest) under a 1 N load. The average values of 10 measurements were recorded, and standard deviations were determined.

## 3. Results and discussion

### 3.1. Thermodynamic modeling

Carbon isopleth with respect to a constant 4Si1Nb composition is given in Fig. 1(a). According to this isopleth, the composition with 3.5wt% C was hypereutectic. Solidification started with graphite (G) precipitation from liquid (L), continued with the precipitation of MC-type carbide, and ended after austenite (A) transformation. Upon cooling, austenite started to transform to ferrite (F), and the transformation was completed at $A_1$ temperature. To understand the effect of aluminum addition on the austenite to ferrite phase transformation, the aluminum isopleth of 3.5C4Si1Nb constant composition is given in Fig. 1(b). According to this isopleth, with increasing aluminum addition, the phase transformation sequence remained the same. In addition, the transformation temperature increased. Understanding the effect of aluminum addition on $A_1$ temperature is important in order to determine the maximum service temperature of the compositions. As given in Fig. 2, aluminum addition increased the $A_1$ temperature due to the solubility of aluminum in ferrite lattice [37]. The $A_1$ temperature of 3.5C4Si1Nb composition (852°C) increased to 960°C by the addition of 4wt% Al in 3.5C4Si1Nb4Al. In commercial SiMo alloys, this temperature has been reported as 820°C [4]. In the studied alloy system, even without aluminum addition, a higher $A_1$ value was achieved.

In high-temperature applications, the thermal stability of the materials should be controlled since a high thermal expansion gradient caused crack formation under thermal cycles [38]. Thus, it is necessary to determine the thermal expansivity of the phase stable up to $A_1$, and using Thermo-Calc, this property as regards the modified alloys can be calculated not only for RT but also for elevated temperature [36]. The variation of the thermal expansivity of ferrite at RT as a function of aluminum content is depicted in Fig. 3(a). The diagram shows that as the aluminum content increased, the thermal expansivity of ferrite increased due to the high solubility of the aluminum in ferrite [39]. The break in the linear relationship at about 3.5wt% Al can be attributed to spin transfers of iron atoms due to impurities such as alumin-

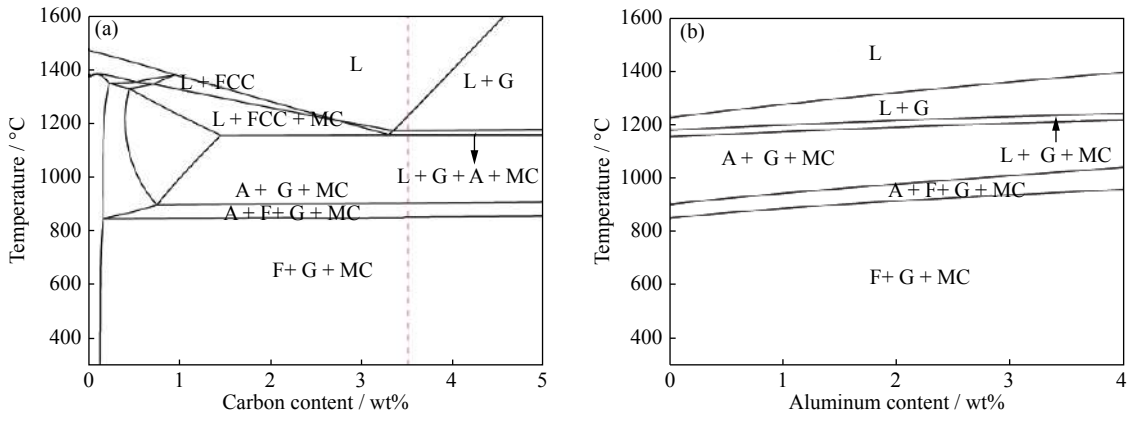


**Fig. 1. C isopleth for 4Si−1Nb (a) and Al isopleth for 3.5C−4Si−1Nb compositions (b).**

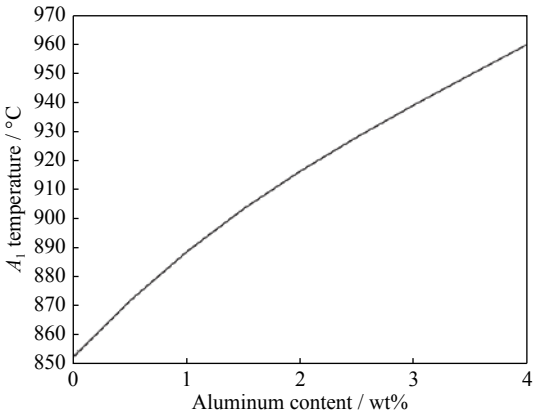


**Fig. 2. Change in $A_1$ temperature as a function of aluminum content.**

um [40]. In the graph, above 3.5wt% Al, the increase in expansivity continues with a similar slope. The dependence of thermal expansivity on temperature is illustrated in Fig. 3(b). For all temperatures, the expansivity increased with the aluminum content. The Fig. 3(b) also shows the increase in $A_1$ temperature by aluminum addition and the linear relationship between temperature and expansivity was limited up to the $A_1$ temperature, above which the transition from body centered cubic (bcc) to face centered cubic (fcc) lattice took place.

Physical properties such as thermal conductivity and thermal expansion coefficient can be affected by not only the matrix phase but also the graphite phase [41–42]. In this context, both the morphology and content of graphite phase as a function of the alloying element should be studied. The variation of graphite content as a function of aluminum addition was calculated, and the obtained data are given in Fig. 4. The diagram shows that aluminum addition had a decreasing effect on graphite content. In solidified cast irons, the accumulation of aluminum atoms around the graphite phases causes nonhomogeneous diffusion of carbon, resulting in a change in its content as well as morphology [6]. The thermal expansivity of the materials used in high-temperature applications is another design criterion, and it must be considered. Calculations indicated that the thermal expansivity of ferrite at RT increased by aluminum addition, limiting the use of the alloy at higher concentration.

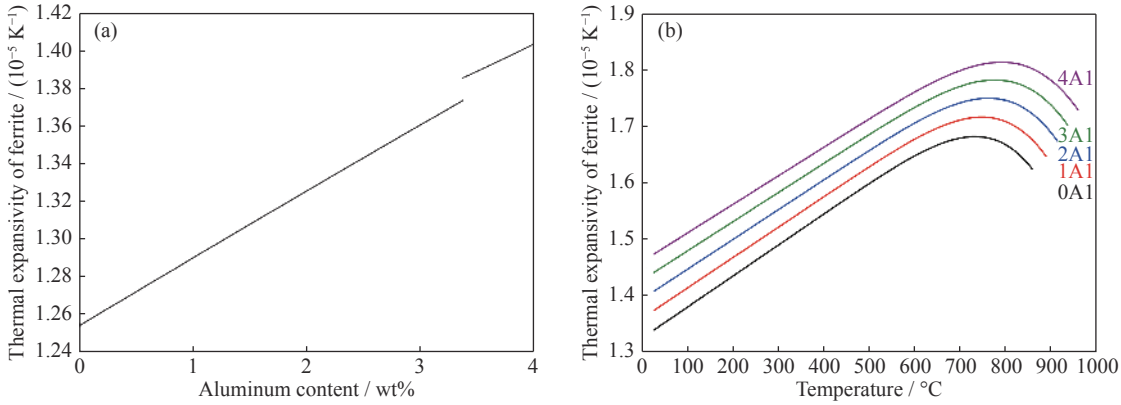


**Fig. 3. Variation of thermal expansivity of ferrite for the studied alloys: (a) as a function of aluminum content; (b) as a function of temperature.**

The analysis of the phase transformation should also be followed by a study of the solidification sequence in order to understand the effect of alloying element on the parameters determining the castability (e.g., liquidus temperature, solidus temperature, and initially solidifying phase). Fig. 5 illustrates the variation of the mole fraction of solid phases calculated using Scheil module under cooling condition with no diffusion in the solid. Fig. 5 also indicates the solidification sequence of the studied compositions, and the calculated values of parameters such as liquidus temperature ($T_L$), crystallization start temperature of graphite ($T_{L+G}$), MC carbide ($T_{L+G+MC}$), austenite ($T_{L+G+MC+A}$), and solidus temperature ($T_S$) are presented in Table 2. The solidification sequence was determined as L → L + G → L + G + MC → L + G + MC + A. The solidification of the 0Al alloy started with graphite precipitation at 1229°C. Moreover, MC-type carbide precipitated from liquid between 1174 and 1160°C due to the Nb content. Finally, austenite transformation started at 1160°C, and solidification ended when austenite transformation was completed at 1148°C. For 1Al, 2Al, 3Al, and 4Al, with increasing aluminum content, the solidification sequence remained the same, and the solidification started at higher temperature: 1278, 1325, 1363, and 1397°C, respectively. All crystallization temperature was affected by aluminum addition; they increased with the increase in aluminum content (Table 2).

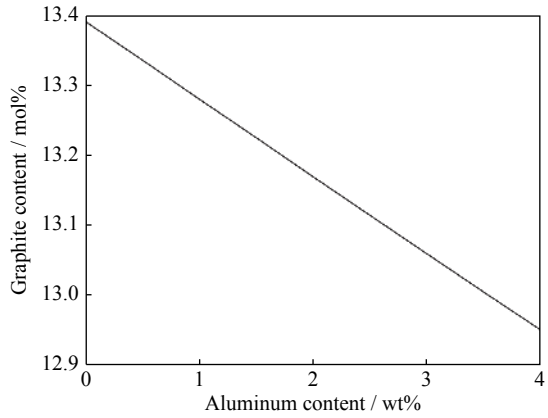


Fig. 4. Effect of aluminum addition on the graphite content.

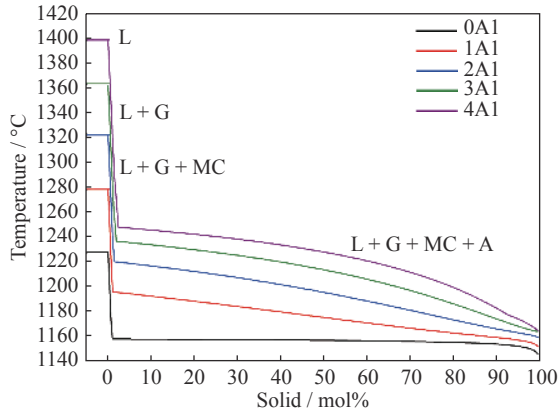


Fig. 5. Solidification paths of 0Al, 1Al, 2Al, 3Al, and 4Al alloys.

Table 2. Calculated solidification parameters for the studied alloys

| Alloy | $T_L$ / °C | $T_{L+G}$ / °C | $T_{L+G+MC}$ / °C | $T_{L+G+MC+A}$ / °C | $T_S$ / °C |
|---|---|---|---|---|---|
| 0Al | 1229 | 1229 | 1174 | 1160 | 1148 |
| 1Al | 1278 | 1278 | 1208 | 1198 | 1157 |
| 2Al | 1325 | 1325 | 1239 | 1221 | 1165 |
| 3Al | 1363 | 1363 | 1267 | 1239 | 1170 |
| 4Al | 1397 | 1397 | 1291 | 1248 | 1172 |

### 3.2. Evaluation of phase transformation by DTA

To validate the Thermo-Calc data, DTA was carried out, and the obtained thermograms for heating and cooling condition are shown in Fig. 6. For the heating condition (Fig. 6(a)), all phase transformations were observed as endothermic peaks at several temperature ranges. For all alloys, the transformation sequence was the same; however, the peaks shifted to higher temperature as aluminum content increased. In DTA, the heating condition allows to investigate the $A_1$ temperature of the modified alloys. The measured $A_1$ temperature was 862, 922, and 962°C for 0Al, 2Al, and 4Al, respectively (Table 3). These values are comparable with the data calculated by Thermo-Calc (Fig. 2). In the cooling condition, with respect to solidification, $T_{L+G}$, $T_{L+G+MC}$, $T_{L+G+MC+A}$, ferrite start temperature ($T_F$), and ferrite finish temperature (equal to $A_1$) could be determined, and all temperatures are listed in Table 3. Compared with the calculated value by Thermo-Calc (Fig. 1(b) and Table 2), the DTA results (Fig. 6(b) and Table 3) under cooling condition revealed lower crystallization temperature; however, there is a certain tendency with respect to aluminum content, as indicated by Thermo-Calc.

### 3.3. Microstructural and mechanical characterization

The metallographically prepared samples at a polished condition were examined using LM to observe the change in graphite content and morphology by aluminum addition. The microstructures are shown in Fig. 7, and the data obtained by

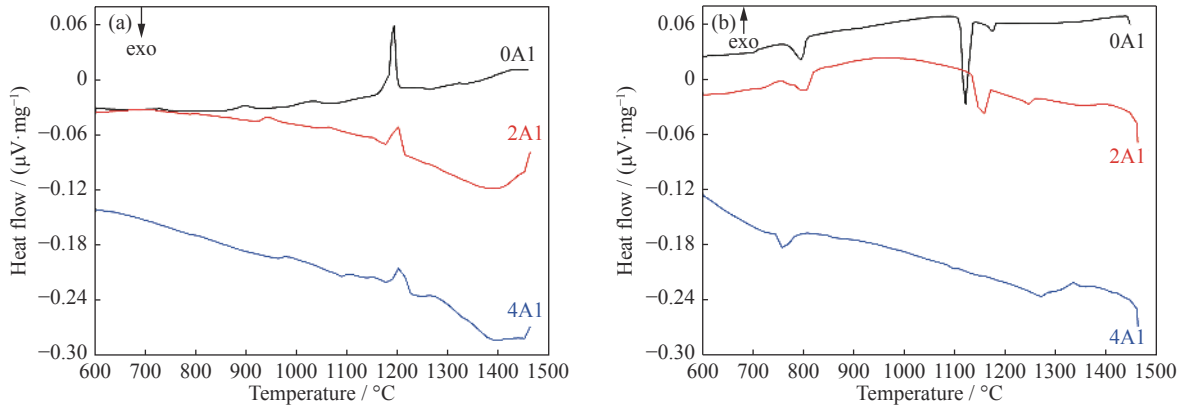


Fig. 6. Thermograms of the cast irons upon different conditions for 0Al, 2Al, and 4Al: (a) heating; (b) cooling.

**Table 3. Critical temperature of the cast irons identified by DTA**

| Alloy | $T_{L+G}$ / °C | $T_{L+G+MC}$ / °C | $T_{L+G+MC+A}$ / °C | $T_F$ / °C | $A_1$ / °C |
|---|---|---|---|---|---|
| 0Al | 1264 | 1182 | 1052 | 1009 | 862 |
| 1Al | 1279 | 1202 | 1192 | 1175 | 894 |
| 2Al | 1330 | 1250 | 1190 | 1043 | 922 |
| 3Al | 1353 | 1267 | 1210 | 1045 | 936 |
| 4Al | 1386 | 1305 | 1245 | 1131 | 962 |

image analysis for content and morphology of graphite are given in Fig. 8 and Table 4, respectively. Fig. 8 shows the decrease in graphite area content with increasing aluminum addition, as predicted by the Thermo-Calc calculations (Fig. 4). The decrease in graphite content by aluminum addition has also been reported by Soiński *et al*. [43]. The morphology of graphite was determined according to DIN EN ISO 945-2. It changed from spheroidal (VI) to irregular spheroidal (V) and vermicular (III) as aluminum content increased (Table 4). A similar observation on the deterioration of nodularity has been reported by Ibrahim *et al*. [6]. This was attributed to the nonhomogeneous and irregular accumulation of Al around the graphite nodules, resulting in a non-uniform diffusion of carbon and the deformation of the graphite morphology [6]. Li showed that by using an effective nodularizer, this deterioration effect could be decreased [44].

The microstructural feature of 0Al alloy is depicted in Fig. 9. As shown in the LM images (Figs. 9(a) and 9(b)), the

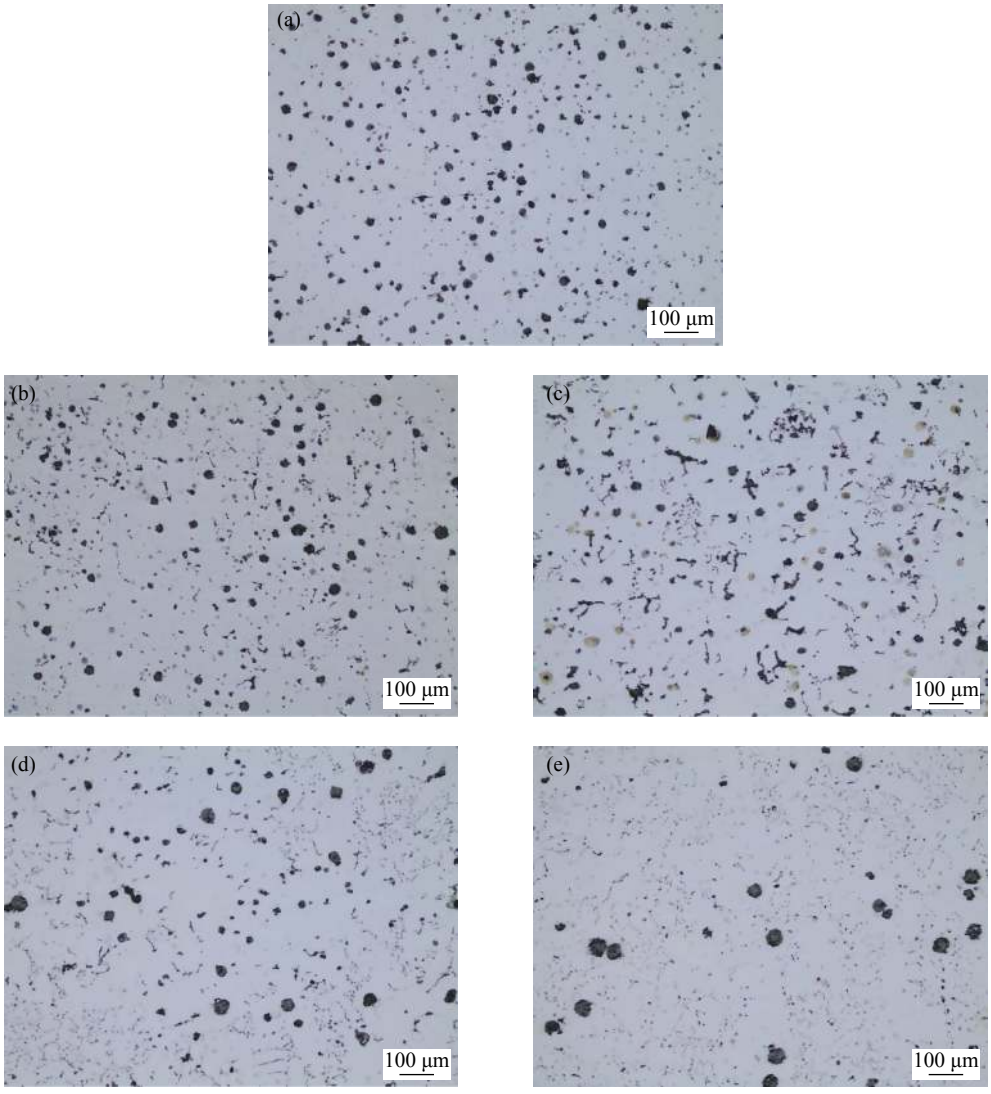


**Fig. 7. LM images showing the graphite morphology in polished cast irons: (a) 0Al; (b) 1Al; (c) 2Al; (d) 3Al; (e) 4Al.**

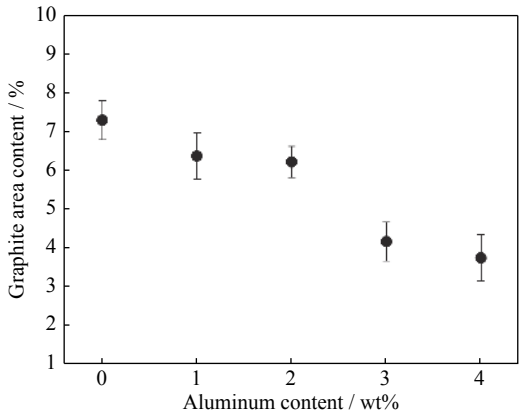


**Fig. 8. Change in graphite area with Al addition.**

matrix consisted of spheroidal graphite, faceted particles (MC carbides), and pearlite (P) embedded in ferrite. The SEM image (Fig. 9(c)) shows both the lamellar structure of pearlite and the blocky structure of Nb-rich MC carbide. All alloys had similar microstructure, which consisted of graphite and carbides in the ferritic matrix (Fig. 10); however, a pearlitic structure was not visible due to the high concentration of silicon and aluminum, as these elements prohibit the formation of pearlite [6,37,45]. The microstructural feature is also validated by XRD data for the selected alloys (Fig. 11). The data confirmed that MC-type carbide is a well-known NbC crystallized in an fcc structure. For the 0Al alloy, no peak indicating pearlite was observed due to the small quantity of this phase.

The aluminum addition not only affected the microstructure but also affected the mechanical properties due to the solid solution hardening provided by the high solubility of

**Table 4. Image analysis results for the graphite area content for different morphologies as determined by DIN EN ISO 945-2** %

| Alloy | Vermicular (III) | Irregular spheroidal (V) | Spheroidal (VI) | Others |
|---|---|---|---|---|
| 0Al | 11.3 | 54.1 | 28.8 | 5.7 |
| 1Al | 14.5 | 54.5 | 26.6 | 7.4 |
| 2Al | 16.2 | 50.1 | 25.3 | 8.4 |
| 3Al | 24.0 | 44.3 | 22.8 | 8.9 |
| 4Al | 20.1 | 48.2 | 19.9 | 11.8 |

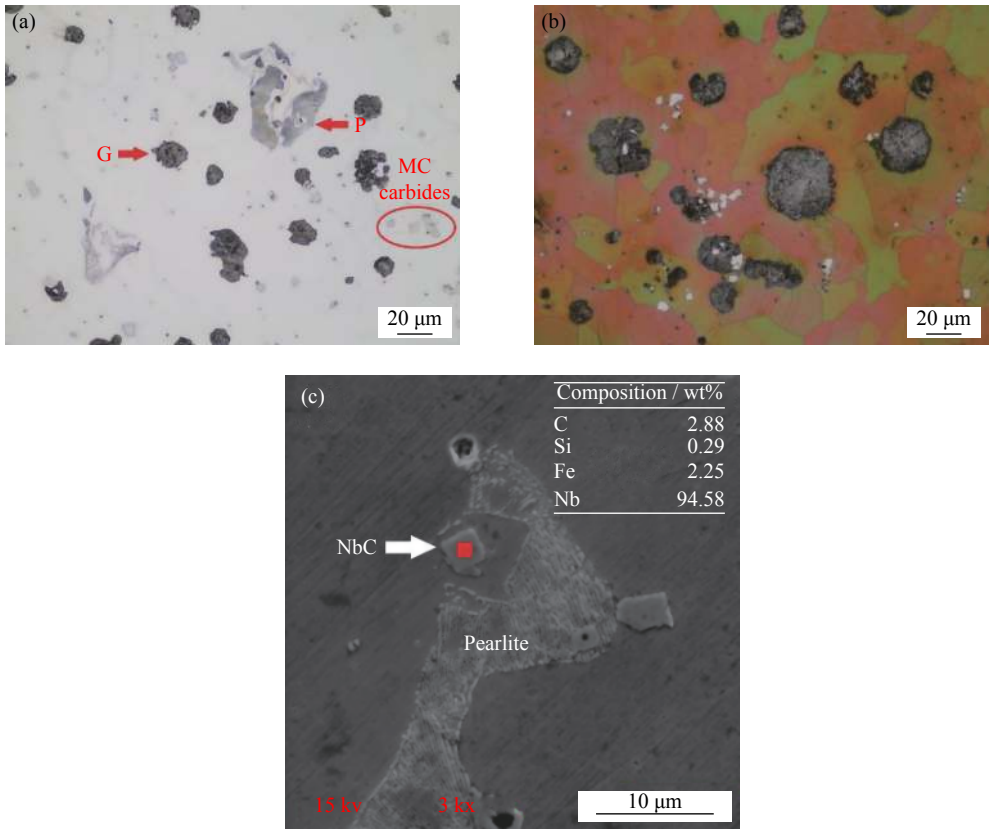


**Fig. 9. Images showing the microstructural feature of 0Al alloy: (a,c) etched using Nital; (b) etched using a composition of 10 g picric acid, 10 g NaOH, 40 g KOH, and 50 mL distilled water.**

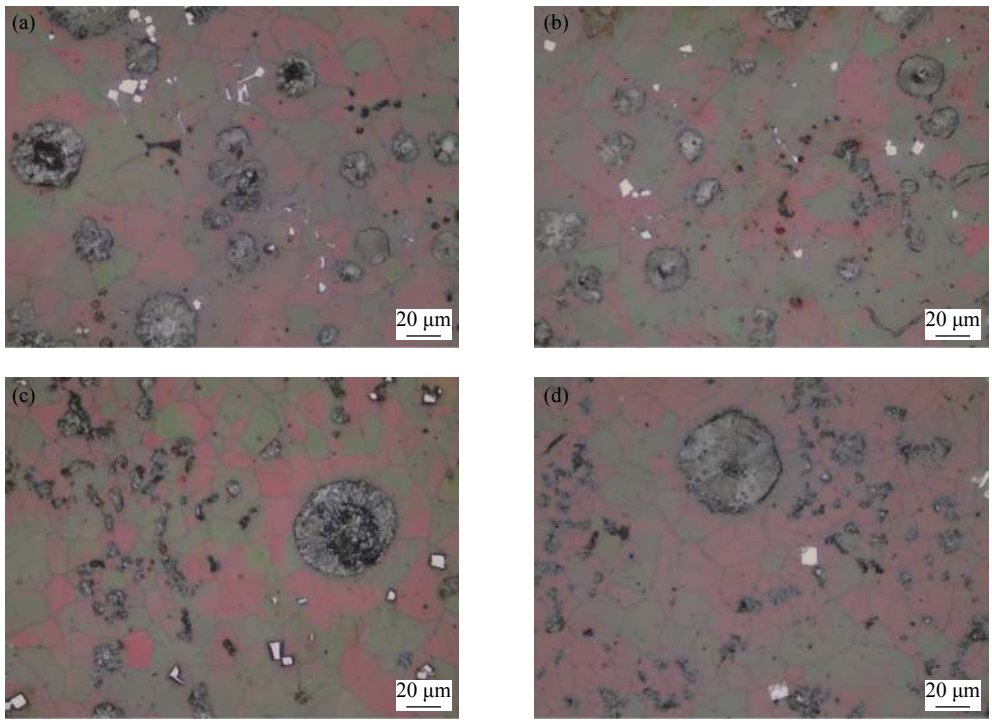


**Fig. 10. LM images showing the microstructure of modified alloys: (a) 1Al; (b) 2Al; (c) 3Al; (d) 4Al.**

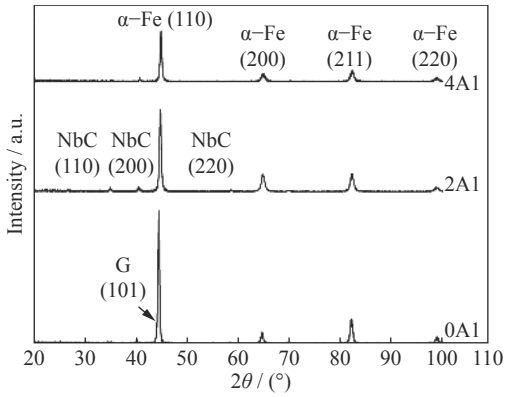


**Fig. 11. XRD patterns of 0Al, 2Al, and 4Al cast irons.**

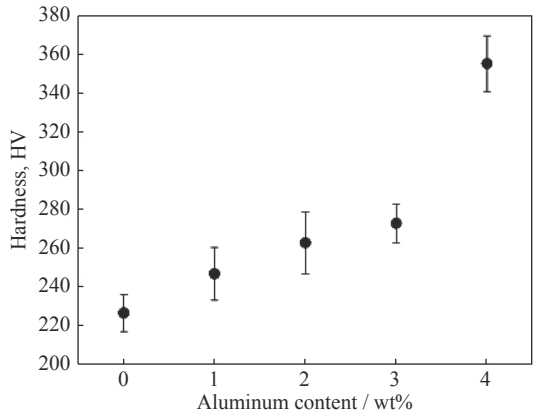


**Fig. 12. Hardness value of cast irons.**

aluminum in ferrite. Hardness measurements revealed this effect (Fig. 12), whereby the hardness increased with aluminum addition. The 0Al alloy had a slightly higher hardness value than the commercial SiMo ductile cast iron [31,46].

## 4. Conclusions

This study aimed to design a novel ductile cast iron composition that can withstand higher operating temperature and costs less than austenitic ductile cast irons and stainless steels, so that it can serve as an alternative to SiMo cast iron. New alloy compositions were designed and thermodynamic calculation was carried out. The calculated data were verified by experimental studies. The whole data revealed the following: (1) for all alloys, the RT phases were graphite, NbC, and ferrite; (2) the $A_1$ temperature of the alloy with 4wt% Al addition reached 960°C, indicating that the alloy can be used at higher temperature, compared to the commercial SiMo; (3) all transformation temperature, including $T_L$, increased with aluminum addition; (4) with the increase in aluminum content, the thermal expansivity of ferrite increased and the graphite content decreased; (5) for all alloys, the solidification sequence was determined as graphite formation from liquid, followed by MC precipitation, and then austenite transformation; (6) with aluminum addition, the graphite content decreased and the graphite nodularity changed from

spheroidal to vermicular.

The current work is a preliminary study on the development of novel cast iron compositions for high-temperature application. It revealed that 4Al alloy has a great potential, compared to the commercial SiMo cast iron. However, further studies will be carried out on these alloys to determine their oxidation behavior, thermal expansion trends, and mechanical properties and decide on the most effective.

## Acknowledegements

The authors, G. Aktaş Çelik, Ş. Polat and Ş. H. Atapek wish to acknowledge the financial support given by Scientific Research Projects Coordination Unit of Kocaeli University under the project No. 2017/118.

## References

[1] A.A. Partoaa, M. Abdolzadeh, and M. Rezaeizadeh, Effect of fin attachment on thermal stress reduction of exhaust manifold of an off road diesel engine, *J. Cent. South Univ.*, 24(2017), No. 3, p. 546.

[2] Y.H. Zhang, M. Li, L.A. Godlewski, J.W. Zindel, and Q. Feng, Creep behavior at 1273 K (1000°C) in Nb-bearing austenitic heat-resistant cast steels developed for exhaust component applications, *Metall. Mater. Trans. A*, 47(2016), No. 7, p. 3289.

[3] M. Ekström and S. Jonsson, High-temperature mechanical- and fatigue properties of cast alloys intended for use in exhaust manifolds, *Mater. Sci. Eng. A*, 616(2014), p. 78.

[4] L.M. Åberg and C. Hartung, Solidification of SiMo nodular cast iron for high temperature applications, *Trans. Indian Inst. Met.*, 65(2012), No. 6, p. 633.

[5] J.P. Shingledecker, P.J. Maziasz, N.D. Evans, and M.J. Pollard, Creep behavior of a new cast austenitic alloy, *Int. J. Press. Vessels Pip.*, 84(2007), No. 1-2, p. 21.

[6] M.M. Ibrahim, A. Nofal, and M.M. Mourad, Microstructure and hot oxidation resistance of SiMo ductile cast irons containing Si–Mo–Al, *Metall. Mater. Trans. B*, 48(2017), No. 2, p. 1149.

[7] Y.H. Zhang, M. Li, L.A. Godlewski, J.W. Zindel, and Q. Feng, Effective design of new austenitic cast steels for ultra-high temperature automotive exhaust components through combined CALPHAD and experimental approaches, *Mater. Sci. Eng. A*, 683(2017), p. 195.

[8] F. Tholence and M. Norell, High temperature corrosion of cast alloys in exhaust environments I-ductile cast irons, *Oxid. Met.*, 69(2008), No. 1-2, p. 13.

[9] M. Ekström, P. Szakalos, and S. Jonsson, Influence of Cr and Ni on high-temperature corrosion behavior of ferritic ductile cast iron in air and exhaust gases, *Oxid. Met.*, 80(2013), No. 5-6, p. 455.

[10] F. Tholence and M. Norell, High temperature corrosion of cast alloys in exhaust environments II-cast stainless steels, *Oxid. Met.*, 69(2008), No. 1-2, p. 37.

[11] Y.H. Zhang, M.L. Larry, L.A. Godlewski, J.W. Zindel, and Q. Feng, Effects of W on creep behaviors of novel Nb-bearing high nitrogen austenitic heat-resistant cast steels at 1000°C, *Mater. Charact.*, 139(2018), p. 19.

[12] M.P. Brady, G. Muralidharan, D.N. Leonard, J.A. Haynes, R.G. Weldon, and R.D. England, Long-term oxidation of candidate cast iron and stainless steel exhaust system alloys from 650 to 800°C in air with water vapor, *Oxid. Met.*, 82(2014), No. 5-6, p. 359.

[13] G.M.C. Güiza, W. Hormaza, A.R. Galvis E, and L.M.M. Morenod, Bending overload and thermal fatigue fractures in a cast exhaust manifold, *Eng. Fail. Anal.*, 82(2017), p. 138.

[14] J.W. Soedarsono, T.P. Soemardi, B. Suharno, and R.D. Sulamet-Ariobimo, Effects of carbon equilavent on the microstructures of thin wall ductile iron, *J. Mater. Sci. Eng.*, 5(2011), No. 3, p. 266.

[15] G.E. Totten, *Steel Heat Treatment Handbook*, Chemical Rubber Company Press, Boca Raton, 2006.

[16] H. Bhadeshia and R. Honeycombe, *Steels: Microstructure and Properties*, Elsevier, Oxford, 2006.

[17] A.R.K. Rashid and D.V. Edmonds, Oxidation behaviur of Al-alloyed ductile cast irons at elevated temperature, *Surf. Interface Anal.*, 36(2004), No. 8, p. 1011.

[18] A. Hassani, A. Habibolahzadeh, and S. Sadeghinejad, Comparison of microstructural and tribological effects of low vanadium–low titanium additions to a gray cast iron, *J. Mater. Eng. Perform.*, 22(2013), No. 1, p. 267.

[19] T.N.F. Souzo, R.A.P.S. Nogueira, F.J.S. Franco, M.T.P Aguilar, and P.R. Cetlin, Mechanical and microstructural characterization of nodular cast iron (NCI) with niobium additions, *Mater. Res.*, 17(2014), No. 5, p. 1167.

[20] Y.Z. Lv, Y.F. Sun, J.Y. Zhao, G.W. Yu, J.J. Shen, and S.M. Hu, Effect of tungsten on microstructure and properties of high chromium cast iron, *Mater. Des.*, 39(2012), p. 303.

[21] C. Delprete and R. Sesana, Experimental characterization of Si–Mo–Cr ductile cast iron, *Mater. Des.*, 57(2014), p. 528.

[22] A. Bedolla-Jacuindde, E. Solis, and B. Hernandez, Effect of niobium in medium alloyed ductile cast irons, *Int. J. Cast Met. Res.*, 16(2003), No. 5, p. 481.

[23] D.X. Zeng, Y.H. Zhang, J.Y. Liu, H.J. He, and X.X. Hong, Characterization of titanium-containing compounds in gray iron, *Tsinghua Sci. Technol.*, 13(2008), No. 2, p. 127.

[24] M. Gómy and M. Kawalec, Effects of titanium addition on microstructure and mechanical properties of thin-walled compacted graphite iron castings, *J. Mater. Eng. Perform.*, 22(2013), No. 5, p. 1519.

[25] X.R. Chen, J. Xu, H. Hu, H. Mohrbacher, M. Kang, W. Zhang, A.M. Guo, and Q.J. Zhai, Effects of niobium addition on microstructure and tensile behavior of as-cast ductile iron, *Mater. Sci. Eng. A*, 688(2017), p. 416.

[26] T. Elbel and J. Hampl, Influence of Al and Ti on microstructure and quality of compacted graphite iron casting, *Metalurgija*, 48(2009), No. 4, p. 243.

[27] M. Gómy and M. Kawalec, Role of titanium in thin wall vermicular graphite iron casting production, *Arch. Foundry*

*Eng.*, 13(2013), No. 2, p. 25.
[28] C.A. Cooper, R. Elliott, and R.J. Young, Investigation of elastic property relationships for flake and spheroidal cast irons using Raman spectroscopy, *Acta Mater.*, 50(2002), No. 16, p. 4037.
[29] H. Nakae and H. Shin, Effect of graphite morphology on tensile properties of flake graphite cast iron, *Mater. Trans.*, 42(2001), No. 7, p. 1428.
[30] D. Holmgren, A. Diószegi, and I.L. Svensson, Effects of nodularity on thermal conductivity of cast iron, *Int. J. Cast Met. Res.*, 20(2007), No. 1, p. 30.
[31] V. Gautam, S. Ahuja, and N. Ram, Design and solidification simulation of exhaust manfold made of SiMo ductile cast iron, *ELK Asia Pac. J.*, (2017), p. 978.
[32] P.H. Huang, J.K. Kuo, T.H. Fang, and W.R. Wu, Numerical simulation and design of casting system for stainless steel exhaust manifold, *MATEC Web Conf.*, 185(2018), p. 8.
[33] B.M. Moon, S.M. Lee, and C.P. Hong, Alloy design for a low thermal expansion cast iron with enhanced mechanical properties, *Int. J. Cast Met. Res.*, 11(1999), No. 6, p. 573.
[34] J.S. Aristeidakis and G.N. Haidemenopoulos, Alloy design based on computational thermodynamics and multi-objective optimization: the case of medium-Mn steels, *Metall. Mater. Trans. A*, 48(2017), No. 5, p. 2584.
[35] U.R. Kattner, The Calphad method and its role in material and process development, *Technol. Met. Mater. Min.*, 13(2016), No. 1, p. 3.
[36] H.L. Lukas, S.G. Fries, and B. Sundman, *Computyational Thermodynamics: The Calphad Method*, Cambridge University Press, New York, 2007.
[37] Y.J. Soo, M.P. Phaniraj, D.I. Kim, J.H. Shim, and M.Y. Huh, Effect of aluminum content on the microstructure and mechanical properties of hypereutectoid steels, *Metall. Mater. Trans. A*, 41(2010), No. 8, p. 2078.
[38] T. Seifert and H. Riedel, Mechanism-based thermomechanical fatigue life prediction of cast iron. part I: models, *Int. J. Fatigue*, 32(2010), No. 8, p. 1358.
[39] C.P. Sharma, *Engineering Materials: Properties and Applications of Metals and Alloys*, New Delhi, Prentice-Hall, 2004.
[40] Z. Yang, X.P. Liu, J. Fu, X.S. Zhao, L.J. Jiang, and S.M. Wang, Thermal expansion properties of Fe−Ni−Co superinvar alloy with Mn, *Chin. J. Rare Met.*, 37(2013), No. 3, p. 501.
[41] Y.Z. Liu, Y.F. Li, J.D. Xing, S.G. Wang, B.C. Zheng, D. Tao, and W. Li, Effect of graphite morphology on the tensile strength and thermal conductivity of cast iron, *Mater. Charact.*, 144(2018), p. 155.
[42] T. Matsushita, E. Ghassemali, A.G. Saro, L. Elmquist, and A.E.W. Jarfors, On thermal expansion and density of CGI and SGI cast irons, *Metals*, 5(2015), p. 1000.
[43] M.S. Soiński, A. Jakubus, and G. Stradomski, The influence of aluminium on the spheroidization of cast iron assessed on the basis of wedge test, *Arch. Foundry Eng.*, 13(2013), No. 2, p. 163.
[44] D.L. Li, Discussion of "microstructure and hot oxidation resistance of SiMo ductile cast irons containing Si−Mo−Al", *Metall. Mater. Trans. B*, 49(2018), No. 2, p. 858.
[45] E. Kozeschnik and H.K.D.H. Bhadeshia, Influence of silicon on cementite precipitation in steels, *Mater. Sci. Technol.*, 24(2008), No. 3, p. 343.
[46] B. Cygan, M. Stawarz, and J. Jezierski, Heat treatment of the SiMo iron castings–case study in automotive foundry, *Arch. Foundry Eng.*, 18(2018), No. 4, p. 103.